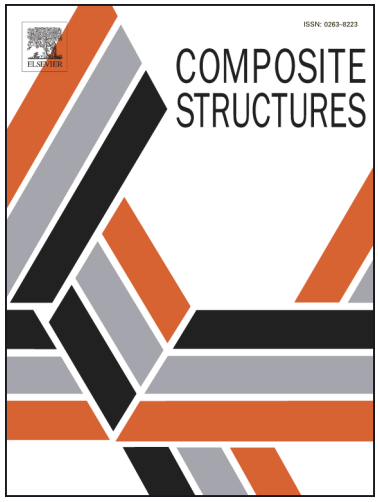

Energy dissipation of nanocomposite based helmets for blast-induced traumatic brain injury mitigation

Daniel Jenson, V.U. Unnikrishnan

PII: S0263-8223(14)00418-8
DOI: http://dx.doi.org/10.1016/j.compstruct.2014.08.028
Reference: COST 5861

To appear in: *Composite Structures*

Received Date: 1 May 2014
Revised Date: 3 August 2014
Accepted Date: 24 August 2014

Please cite this article as: Jenson, D., Unnikrishnan, V.U., Energy dissipation of nanocomposite based helmets for blast-induced traumatic brain injury mitigation, *Composite Structures* (2014), doi: http://dx.doi.org/10.1016/j.compstruct.2014.08.028

Energy Dissipation of Nanocomposite Based Helmets for Blast-induced Traumatic Brain Injury Mitigation

Daniel Jenson and V. U. Unnikrishnan[§]
Department of Aerospace Engineering and Mechanics
The University of Alabama, Tuscaloosa, AL 35487-0280
[§] *e*-mail: vunnikrishnan@ua.edu

Abstract

Injuries caused to the head by ballistic shock waves during blast impacts are not well understood. It has been postulated that traumatic brain injury (TBI) can be caused when the blast wave causes the kinetic energy and the pressure in the main blood vessels to oscillate rapidly and travel to the brain thereby damaging the axonal fibers and neurons or with the direct wave transmission to the head. In the direct wave transmission, the severity of blast wave impact can be reduced by ballistic helmets. The ballistic helmets currently used in the military have been designed to provide protection against penetrating ballistic projectiles and their effectiveness against blast shock wave has not been thoroughly understood. This research would focus on developing a multiscale computational model of blast impact response of high-performance nanocomposite materials for the helmet, followed by estimation of blast energy transfer to the tissues in the human head. Such a combined atomistic-computational model of ballistic response of nanocomposites, coupled with a human morphology-specific computational model is necessary to study the mechanics of blast impact on human head.

Keywords: Blast-induced Traumatic Brain Injury, Multiscale Analysis, Mathematical Homogenization, Molecular Dynamics

1. Introduction

The skull protects the brain, which is the most sensitive organ, from injuries during fall, stroke or blast wave impacts. Traumatic brain injury (TBI), or intra-cranial injury, is the damage caused to the brain by external mechanical forces, resulting in permanent or temporary impairment of the brain functions [1]. Blast injury is caused by a sudden increase

in air pressure and causes injuries in spaces containing gas [2]. In a blast, shock wave travels at the speed of sound, and air is accelerated by this shock wave, forming a high-velocity blast wind. It has been found that during Operation Enduring Freedom and Operation Iraqi Freedom, improvised explosive devices (IEDs), and roadside car bombs caused about 60% of US casualties in Iraq and about 50% in Afghanistan [3]. Blast-induced TBIs have now become extremely significant as studies have shown that between January 2003–2005, out of the 450 soldiers admitted to Walter Reed Army Medical Center, 59% were diagnosed with TBI of which 56% were considered moderate to severe, and 44% were considered mild [4, 5].

There are several causes of blast-induced TBI. Primary blast injury is caused by a high-pressure shock wave interacting with the body [3]. This shock wave produces high pressure, which can be amplified due to the impedance mismatch between the skull and air [6]. The direct impact of the shock wave causes acceleration of the head, and since the inertia of the brain is less than the inertia of the skull, the brain continues to vibrate after the skull has stopped moving. Cavitation bubbles are then formed from the intracranial pressure changes [3] and these bubbles cause injury to the brain as they collapse. In cases when the head is not directly subjected to the blast, the shock wave can be transferred through the abdomen to the blood vessels or other fluid pathways in the thoracic region. This compression effect can cause waves, which transmit kinetic energy to the brain [7]. Another cause of traumatic brain injury is due to shrapnel and debris from explosions. This is called secondary blast injury, and can often go further than the primary high pressure blast wave. The acceleration of the different body parts by the blast wind can cause tertiary blast injuries as well. Due to the difference in inertia between the skull and brain, higher shearing strains form in the intra-cranial region, causing shearing injuries [3]. Further, the high pressure gases following the explosion are at very high temperatures and these hot gasses can cause quaternary injuries, which include pulmonary injuries from the toxic gas and burns and the brain may also be damaged if the skull is heated excessively.

Various models have been created to simulate blast waves impacting a human head. A

finite element (FE) study was initially carried out that could be parameterized to allow for various head sizes [8]. Grujicic et al. demonstrated the use of a Lagrangian-domain model for a human head to simulate blast-induced traumatic brain injury. They obtained results for pressure and stress measured at different points in the head model [9]. Experimental tests often demonstrated the need of helmets which can absorb blast pressure and thus mitigate the effects of blast impact on the human brain. At the same time, these helmets must protect the head from blunt trauma caused by shrapnel-induced wounds. Ganpule et al. performed finite element analysis on the role of the helmet in mitigating blast shock wave propagation [10]. They concluded that the highest reflected overpressure when a shock wave impacts a human head are in the regions of concavity, especially at the nasion, which is the nose-eye cavity. Kulkarni et al. carried out a comparative study on ballistic helmets [3]. This review included helmet materials such as Kevlar K29, K129 fibers, and thermoset resins, and possible future materials to be used for helmets, such as thermoplastic polymers and nano-composites.

The use of Kevlar-Carbon Nanotube based composites for use in helmets is hypothetical; however, there have been numerous studies on Kevlar-nanocomposites [11] for various applications like velocity impact studies and it was found that the energy absorption and impact response characteristics of the composite is increased due to the presence of nanotubes [12]. Similar trends were also observed by Randjbaran et al [13] for the ballistic energy absorption of hybrid composite laminates reinforced with Kevlar and nanotubes.

Nanocomposite materials are often better alternatives to traditional composite materials because of their excellent mechanical properties: high stiffness-to-weight, strength-to-weight ratios, and excellent structural deformation characteristics. However, the major deterrent to experimental investigation of novel nanocomposites in the helmet design is the extreme cost and the lack of understanding of material response under extreme conditions. This handicap can only be overcome by developing multiscale computational models that consider the influence of materials at the nanoscales and macroscales. In this work, we develop a

multiscale computational model of the helmet material with reinforced carbon nanotubes. The nanocomposite-based helmet material would be studied to understand the effect of energy transfer to the brain under blast loading conditions. The rest of the paper is as follows, Section 2 consists of the development of the computational model of the human head and the representation of the blast wave. This section is followed by the discussion of numerical results on the amount of energy transfer from the blast to the brain in a protected and unprotected head and also with a nanocomposite helmet. The paper concludes with a discussion of results.

2. Ideal-blast Waves

There are many sources of blasts that occur in a battle-field that produces pressure waves by rapid release of energy. Explosion sources also occur during the rapid vaporization of thin metal films or fine wires. However, more well-known blast sources are from chemical or nuclear reactions, when a sudden increase in air pressure causes a shock wave to form. This shock front is almost instantaneous and causes nearly discontinuous increases in temperature, density, and pressure [14]. A pressure wave can be approximated using a Friedlander equation, which can be used to describe the physical properties of an ideal blast shock wave as given by Equation (1) [15, 16] (see Figure 1). The most efficient means of representing a blast impact is by the use of data from ConWep. ConWep is a collection of calculation routines that characterizes the effect of conventional weapons that includes air blast routines, breach, cratering, ground shock, and fragment and projectile penetrations etc. [17, 18].

$$P = P_s e^{-\frac{t}{t^*}} \left(1 - \frac{t}{t^*}\right) \tag{1}$$

3. Computational Model of Human Head and Helmet

The 3D FE computational models are developed from the medical image data to create STereoLithography (.stl) files [19]. The FE model of the human head was obtained from the

MR/CT data obtained from the Visible Human Female database from the National Library of Medicine [20]. This study partially follows the process outlined by Vonach et al. for creating the model of the human head [19]. Following the creation of the geometric model, tetrahedral or hexahedral meshing algorithms are used to generate the equivalent finite element mesh. The MR/CT images were then converted to a FE mesh using segmentation followed by smoothening of the resulting STL files and final conversion into an FE mesh. FE analysis was carried out using the general purpose FE code Abaqus (Abaqus Version 6.12, Dassault Systmes) to study the effects of blast induced pressure differences in the human head with and without an helmet, using ConWep blast loading. The ConWep implementation in Abaqus is used for the simulations. The FE geometry of the human head model includes the brain, surrounding cerebral spinal fluid, and the skull. In the FE model, the head is fixed at the base of the neck with encastre boundary conditions. The model consists of the skull having 5998 elements, the cerebral spinal fluid with 5352 elements, and the brain model contains 6745 elements, for a total of 18095 elements of type C3D4. In this study, the heterogeneity of the brain material and its non-isotropic behavior is not taken into account. A Mooney-Rivlin model is considered for the brain [21] and the strain energy function is given by [22, 23]:

$$W = C_{10}(J_1 - 3) + C_{01}(J_2 - 3) + \frac{1}{D_1}(J_{el} - 1)^2 \tag{2}$$

where W is the strain energy potential, J_{el} is the elastic volume ratio, J_1 is the first invariant of the deviatoric strain, J_2 is the second invariant of the deviatoric strain, and C_{10}, C_{01}, and D_1 are material constants dependent on temperature. Linear viscoelasticity [24] is used to estimate the second Piola-Kirchhoff stress by the following convolution integral [21]:

$$S_{ij} = \int_0^t G_{ijkl}(t - \tau)\frac{\delta E_{kl}}{\delta \tau} d\tau \tag{3}$$

where S_{ij} is the second Piola-Kirchhoff stress, $G_{ijkl}(t - \tau)$ is the relaxation modulus for the

different stress measures, and E_{kl} is the Greens strain tensor. The Cauchy stress $\boldsymbol{\sigma}$ (σ_{ij}) can be obtained from the Second Piola-Kirchoff stress from [22]

$$\boldsymbol{\sigma} = \frac{1}{J}\mathbf{F} \cdot \mathbf{S} \cdot \mathbf{F}^T \tag{4}$$

where $\mathbf{F}$ is the deformation gradient tensor, and J is the Jacobian of transformation. Finally, this stress is superimposed to the stress tensor which was determined from the strain energy function. A Prony series can be used to represent the relaxation modulus for an isotropic material as follows [21]:

$$G(t) = G_0 + \sum_{i=1}^{n} G_i e^{-\beta_i t} \tag{5}$$

where β_i is the decay constant and G_i is the relaxation modulus. The parameters selected for the brain are density of 1040 kg/m^3 [9] with Mooney-Rivlin coefficients C_{10} = 3102.5 Pa, C_{01} = 3447.2 Pa, and D_1 = 1.095 GPa from a bulk modulus of 2.19 GPa [21]. The cerebral spinal fluid is modeled using fluid-like properties using the linear U_s–U_p equation of state (EOS), with the final Hugoniot pressure used as the constitutive relationship. U_s is the shock velocity and U_p is the particle velocity and it can be considered that a linear relationship exists between the shock velocity and particle velocity given by $U_s = c_0 + sU_p$. In this linear relationship, $\dot{p} = -K\dot{\varepsilon}_{ij}$, where K is the bulk modulus of elasticity, $\dot{p}$ is the pressure rate, and $\dot{\varepsilon}_{ij}$ is the deviatoric strain rate [21]. The linear form is given by:

$$p = \frac{\rho_0 c_0^2 \eta}{(1 - s\eta)^2}(1 - \frac{\Gamma_0 \eta}{2}) + \Gamma_0 \rho_0 E_m \tag{6}$$

The linear response described here is obtained by setting the parameters s = 0.0 and Γ_0 = 0.0 since $K = \rho_0 c_0^2$ for small strains. This gives a c_0 of 1451.127 m/s using a bulk modulus of 2.19 GPa [21] and the density is taken as 1000 kg/m^3. The skull is considered as a linear elastic material and is modeled based on Mori-Tanaka(M-T) [25] based homogenization of a porous bone structure. For an elastic composite material, the effective constitutive relations are given by the volume average of the stress and strain. Similarly, for each phase

on the microscale, the constitutive relation can be given as:

$$\langle \sigma \rangle_{tot}^{k} = C^{k} \langle \varepsilon \rangle_{tot}^{k} \tag{7}$$

where $\langle . \rangle_{tot}^{k}$ is the volume averaged state of phase, including the matrix, fiber and any interphase layers [26]. The volume averaging $\langle . \rangle$ of the state variables for an equivalent continuum (EC) are given by

$$\langle \bar{\sigma}_{\alpha\beta} \rangle_{EC} = \frac{1}{V} \int_{\Omega} \sigma_{\alpha\beta} dv; \;\; \langle \bar{\varepsilon}_{\alpha\beta} \rangle_{EC} = \frac{1}{V} \int_{\Omega} \varepsilon_{\alpha\beta} dv; \;\; \langle \bar{\sigma}_{\alpha\beta} \rangle_{EC} = C \langle \bar{\varepsilon}_{\alpha\beta} \rangle_{EC} \tag{8}$$

and for an N-particle atomic ensemble we have: $\langle \bar{\sigma}_{\alpha\beta} \rangle = \frac{1}{N} \sum_{i=1}^{N} \sigma_{\alpha\beta}$; $\langle \bar{\varepsilon}_{\alpha\beta} \rangle = \frac{1}{N} \sum_{i=1}^{N} \varepsilon_{\alpha\beta}$.

The porosity of the skull bone is taken as 0.82, which is that of a cancellous bone and having a Poisson's ratio of 0.32, with a Young's modulus of 22.0 GPa [27] for the matrix material. The density of the skull bone is taken as 1412 kg/m^3 [9]. The effective Young's modulus and Poisson's ratio of the composite bone (porous) tissue using Mori-Tanaka method is given by Equations (9)-(12) [28] and the homogenized modulus of the skull is taken as 2.174 GPa, with Poisson's ratio of 0.253 and porosity of 0.82 [27].

$$\overline{E} = 2\overline{\mu} \left[1 + \frac{3\overline{K} - 2\overline{\mu}}{2(3\overline{K} + \overline{\mu})} \right] \tag{9}$$

where

$$\overline{K} = K_0 \left\{ 1 + \frac{c(K_1 - K_0)}{K_0 + 3\gamma_0(1-c)(K_1 - K_0)} \right\} \tag{10}$$

$$\overline{\mu} = \mu_0 \left\{ 1 + \frac{c(\mu_1 - \mu_0)}{\mu_0 + 2\delta_0(1-c)(\mu_1 - \mu_0)} \right\} \tag{11}$$

where, $\gamma_0 = \frac{1+V_0}{9(1-V_0)}$; $\delta_0 = \frac{4-5V_0}{15(1-V_0)}$; $K_n = \frac{E_n}{3(1-2\nu_n)}$ and $\mu_n = \frac{E_n}{2(1+\nu_n)}, n = 0, 1$

$$\overline{\nu} = \frac{3\overline{K} - \overline{E}}{6\overline{K}} \tag{12}$$

The helmet made of thermoset resin/KevlarK129 composite, with density 1440 kg/m^3, effective Young's modulus of 1.24 GPa, and Poisson's ratio of 0.36 is used in the simulations [29] (as shown in Table 1). The inner padding is considered to have a density of $136kg/m^3$, with a Young's modulus of 8.0 MPa, and Poisson's ratio of 0.2 [29]. Additionally we consider a carbon nanotube reinforced thermoset resin also to understand the energy dissipation characteristics of the helmet material.

Table 1: Properties of skull, brain and helmet material used in computational simulations

Material	Elastic (E)/Bulk (K) Modulus	Poisson's ratio	Density (kg/m^3)
Brain Tissue	K = 2.19 GPa		1040
Skull	E = 2.174 GPa	0.253	1412
Helmet (KevlarK129)	E = 1.24 GPa	0.36	1440

The Young's modulus of a (5, 5) single-walled carbon nanotube was calculated using LAMMPS, a molecular dynamics simulator. It should be emphasized that atomistic simulations are carried out only on the CNT and not on a Kevlar-CNT ensemble and it is assumed that the properties of the CNT obtained from the MD simulations would bridge the scales from the atomistic to the continuum. In MD simulations, the motion of particles in an atomistic system is governed by the Hamiltonian, which is a function of the position and momentum of the particles, and the Hamiltonian equations of motion. The Hamiltonian represents the total energy of an isolated system and is composed of the sum of the potential and kinetic energy and the thermodynamic terms

$$\mathrm{H}\left(r^N, p^N\right) = \frac{1}{2m}\sum_i p_i^2 + U\left(r^N\right) \tag{13}$$

where $U\left(r^N\right)$ is the potential energy from intermolecular interactions as a function of the spatial ordinate r^N, $\frac{1}{2m}\sum_i p_i^2$ represents the momentum p of the particle i with mass m_i, which is a function of the absolute temperature called the kinetic energy. The time derivative of the Hamiltonian gives

$$\frac{d\mathrm{H}}{dt} = \frac{1}{m}\sum_i p_i.\dot{p}_i + \sum_i \frac{\partial U}{\partial r_i}.\dot{r}_i = 0 \tag{14}$$

and with the spatial derivative we obtain the equation of motion

$$\frac{d\mathrm{H}}{dr_i} = \frac{\partial U}{\partial r_i} \tag{15}$$

The total potential of the nanotube structure is given by the sum of valence bond energies and the nonbonding interactions [30, 31, 32]

$$U^{tot} = \sum_j \sum_{j>i} \left[V_{ij}^B + V_{ij}^{NB}\right] \tag{16}$$

where V_{ij}^B is the potential energy due to bonding and V_{ij}^{NB} is the potential energy due to nonbonding interactions. The reliability of an MD simulation depends mainly on the type of potential functions. Empirical bond–order potentials of the Reactive Empirical Bond Order (REBO) Potential of Brenner type are found to be excellent for the simulation of carbon based materials [33, 34, 35]. These types of potentials are capable of describing the changes in the bonding in a system but lacks in describing long range interactions, which are often neglected [36]. The Adaptive Intermolecular Reactive Empirical Bond Order (AIREBO) Potential has been used in the simulations [37]. The total potential energy of an atom in an AIREBO potential is given by

$$U = \frac{1}{2}\sum_i \sum_{j\neq i} \left[E_{ij}^{REBO} + E_{ij}^{LJ} + \sum_{k\neq i,j} \sum_{l\neq i,j,k} E_{kijl}^{TORSION}\right] \tag{17}$$

here E_{ij}^{REBO} represents the Reactive Empirical Bond-Order (REBO) Potential and E_{ij}^{LJ} represents the non-bonded interactions and $E_{kijl}^{TORSION}$ represents the torsional component of the potential function. The force of attraction and repulsion ($F_{\alpha\beta}$) experienced by each molecule is obtained from the gradient of the potential field.

$$F_{\alpha\beta} = -\frac{\partial U^{tot}}{\partial r_{\alpha\beta}} \tag{18}$$

The molecular dynamics simulations included a minimization of the input system, an equilibration to 300 K for 30000 steps, and a deformation test for 20000 steps at a strain rate of 0.01 ps^{-1}. Each time step was taken as 0.2 fs and uses a reactive AIREBO potential function developed by Stuart et al. for the modeling of intermolecular interactions and chemical reactions in a condensed-phase hydrocarbon system [37]. The Young's modulus of the carbon nantoube was estimated to be 1.004 TPa and it closely matches the values reported in literature of 1 TPa, with a Poisson's ratio of 0.14 [38] and having a density of 1330 kg/m^3 [39]. A 5% volume fraction of the carbon nanotube was assumed in the analysis and the resulting composite is considered to have an effective Young's modulus of 1.3772 GPa, an effective Poisson's ratio of 0.35, with a density of 1434.5 kg/m^3.

4. Numerical Results and Discussion

Three different magnitudes of explosion are modeled using the ConWep blast loading pressure wave as shown in Figure 2, at a distance of 0.8 m in front of the head model. The coup side corresponds to the site of impact of the explosion, which in this case is the front of the brain.

The maximum shear stress was found to be 23.2 kPa for 0.038 kg blast loading and with 0.093 kg of TNT, the maximum shear stress was obtained as 53.4 kPa. For 0.227 kg explosion, the maximum shear stress was obtained as 90.9 kPa and these compares well with the simulations carried out by Chafi et al. [21], with increasing discrepancy for larger blast loading, and are attributed to the difference in the model development from the MRI data. The coup shear stress for the brain for the three different explosions, measured with respect to time is indicated in Figure 3. Simulations are further carried out for the same magnitudes of TNT exploding, at a distance of 0.8 m to the rear of the head. The roles of the coup and countercoup sites are now reversed as the detonation is now performed at the rear of the

head and as shown in Figures 4, the maximum principal stress at the coup and countercoup sites are found to be significantly higher at the coup site.

A helmet is now added to the head model with a padding on the inside. Similar simulations were carried out to demonstrate the efficacy of the helmet in mitigating the effects of shock waves impacting the human head. The results obtained from detonations occurring at the front of the head are compared to an unprotected head model and the different magnitudes of the maximum principal stress were obtained for pristine helmet material as shown in Figure 5. The principal stresses are compared from an unprotected head to that of a protected head as shown in Figure 6 and it can be seen that for highest load of 0.227 kg TNT, the maximum principal stress is significantly reduced for the protected head when compared to the unprotected head. This difference was not significant for higher loads, which indicate that greater amount of stresses are transferred to the brain tissue as the impact pressure gets higher.

The efficacy of the helmet in protecting the brain from blast-induced TBI can be measured in terms of the transfer of strain energy density (SED). SED is the amount of strain energy stored per unit volume. Simulations were performed to calculate the energy density for the three different magnitudes of explosions. Figures 7, 8 and 9 indicate the energy density at the front of the brain (coup site) for the porous unprotected head model (M-T model skull), the head protected by the ACH, and the head protected by the CNT–enhanced helmet. It can be seen that the energy density was greatly reduced when the unprotected head is compared to the head with the advanced combat helmet and the carbon nanotube–enhanced helmet material. This indicates that significant energy is absorbed by the helmet and less shock energy per unit volume reaches the brain. However, the same discrepancies discussed previously are seen when comparing the CNT-enhanced helmet with the original Advanced Combat Helmet (ACH). This discrepancy can be rectified by considering the use of an energy dissipation-based material model for the analysis.

5. Conclusions

Head injuries by ballistic shock waves during blast impacts are not well understood and the damage to the brain tissue leads to inevitable neurological effects that can be very slow to appear. The ballistic helmets currently used in the military have been designed for protection against penetrating ballistic projectiles and their effectiveness against blast wave has not been thoroughly understood. The major outcome of this study is the development of an enhanced computational model that helps in our understanding of blast-induced TBI and exploring the possibility of mitigation of head injury using nanocomposite materials in helmets.

6. Acknowledgment

The second author would like to acknowledge the faculty start up funds and the Research Grants Committee 2014-seed grants from The University of Alabama.

7. References

[1] Okie, Susan, Traumatic brain injury in the war zone, New England Journal of Medicine 352 (20) (2005) 2043–2047.

[2] Mellor, Adrian J. and Woods, David, Serum neutrophil gelatinase-associated lipocalin in ballistic injuries: A comparison between blast injuries and gunshot wounds, Journal of Critical Care 27 (4) (2012) 419.e1–419.e5.

[3] Kulkarni, S. G. and Gao, X. L. and Horner, S. E. and Zheng, J. Q. and David, N. V., Ballistic helmets – their design, materials, and performance against traumatic brain injury, Composite Structures 101 (0) (2013) 313–331.

[4] Hoge, Charles W. and McGurk, Dennis and Thomas, Jeffrey L. and Cox, Anthony L. and Engel, Charles C. and Castro, Carl A., Mild traumatic brain injury in u.s. soldiers returning from iraq, New England Journal of Medicine 358 (5) (2008) 453–463.

[5] Sundaramurthy, A. and Alai, A. and Ganpule, S. and Holmberg, A. and Plougonven, E. and Chandra, N., Blast-induced biomechanical loading of the rat: an experimental and anatomically accurate computational blast injury model, Journal of neurotrauma 29 (13) (2012) 2352–2364.

[6] Alley, Matthew D. and Schimizze, Benjamin R. and Son, Steven F., Experimental modeling of explosive blast-related traumatic brain injuries, NeuroImage 54, Supplement 1 (0) (2011) S45–S54.

[7] Courtney, A. C. and Courtney, M. W., A thoracic mechanism of mild traumatic brain injury due to blast pressure waves, Medical Hypotheses 72 (1) (2009) 76–83.

[8] Kleiven, Svein and von Holst, Hans, Consequences of reduced brain volume following impact in prediction of subdural hematoma evaluated with numerical techniques, Traffic Injury Prevention 3 (4) (2002) 303–310.

[9] Grujicic, M and Bell, WC and Pandurangan, B and He, T, Blast-wave impact-mitigation capability of polyurea when used as helmet suspension-pad material, Materials & Design 31 (9) (2010) 4050–4065.

[10] Ganpule, S. and Gu, L. and Alai, A. and Chandra, N., Role of helmet in the mechanics of shock wave propagation under blast loading conditions, Computer Methods in Biomechanics and Biomedical Engineering 15 (11) (2011) 1233–1244.

[11] Sainsbury, Toby and Erickson, Kris and Okawa, David and Zonte, C. Sebastian and Frechet, Jean M. J. and Zettl, Alex, Kevlar functionalized carbon nanotubes for next-generation composites, Chemistry of Materials 22 (6) (2010) 2164–2171.

[12] Iman Taraghi and Abdolhossein Fereidoon and Fathollah Taheri-Behrooz, Low-velocity impact response of woven kevlar/epoxy laminated composites reinforced with multi-walled carbon nanotubes at ambient and low temperatures, Materials & Design 53 (2014) 152 – 158.

[13] Randjbaran, Elias and Zahari, Rizal and Abdul Jalil, Nawal Aswan and Abang Abdul Majid, Dayang Laila, Hybrid composite laminates reinforced with kevlar/carbon/glass woven fabrics for ballistic impact testing, The Scientific World Journal 2014 (2014) Article ID 413753, 7.

[14] Baker, Wilfred Edmund, Explosions in air, University of Texas Press Austin, 1973.

[15] Tan, K. T. and Huang, H. H. and Sun, C. T., Blast-wave impact mitigation using negative effective mass density concept of elastic metamaterials, International Journal of Impact Engineering 64 (2014) 20–29.

[16] Dewey, John M, The shape of the blast wave: studies of the friedlander equation, in: International Symposium on Military Aspects of Blast and Shock, Jeruzalem, Israel, 2010.

[17] Ostraich, B and Sadot, O and Levintant, O and Anteby, I and Ben-Dor, G, A method for transforming a full computation of the effects of a complex-explosion scenario to a simple computation by conwep, Shock Waves 21 (2) (2011) 101–109.

[18] Ian G. Cullis and James Schofield and Angela Whitby, Assessment of blast loading effects types of explosion and loading effects, International Journal of Pressure Vessels and Piping 87 (9) (2010) 493 – 503.

[19] Vonach, Martin and Marson, Ben and Yun, Mark and Cardoso, Jorge and Modat, Marc and Ourselin, Sebastien and Holder, David, A method for rapid production of subject specific finite element meshes for electrical impedance tomography of the human head, Physiological Measurement 33 (5) (2012) 801.

[20] Ackerman, Michael J, Accessing the visible human project, D-Lib Magazine 1 (4).

[21] Chafi, MS and Karami, G and Ziejewski, M, Biomechanical assessment of brain dynamic responses due to blast pressure waves, Annals of biomedical engineering 38 (2) (2010) 490–504.

[22] Reddy, J. N., Introduction to Continuum Mechanics: With Applications, Cambridge University Press, New York, NY, 2008.

[23] Unnikrishnan, G. U. and Unnikrishnan, V. U. and Reddy, J. N., Finite element model for nutrient distribution analysis of a hollow fiber membrane bioreactor, International Journal for Numerical Methods in Biomedical Engineering 28 (2) (2012) 229–238.

[24] Wang, Xin and Schoen, Jonathan A. and Rentschler, Mark E., A quantitative comparison of soft tissue compressive viscoelastic model accuracy, Journal of the Mechanical Behavior of Biomedical Materials 20 (0) (2013) 126–136.

[25] Mori, T. and Tanaka, K., Average stress in matrix and average elastic energy of materials with misfitting inclusions, Acta Metallurgica 21 (5) (1973) 571–574.

[26] Unnikrishnan, G. U. and Unnikrishnan, V. U. and Reddy, J. N., Constitutive material modeling of cell: A micromechanics approach, Journal of Biomechanical Engineering 129 (3) (2007) 315–323.

[27] Gilbert, Robert P. and Guyenne, Philippe and Li, Jing, A viscoelastic model for random ultrasound propagation in cancellous bone, Computers & Mathematics with Applications 66 (6) (2013) 943–964.

[28] Qu, Jianmin, The effect of slightly weakened interfaces on the overall elastic properties of composite materials, Mechanics of Materials 14 (4) (1993) 269–281.

[29] Jason, Amanda Marie, Facial protective devices for blast-induced traumatic brain injury mitigation, Ph.D. thesis (2010).

[30] Sears, A. and Batra, R. C., Macroscopic properties of carbon nanotubes from molecular-mechanics simulations, Physical Review B (Condensed Matter and Materials Physics) 69 (23) (2004) 235406–10.

[31] Mylvaganam, K. and Zhang, L., Nanotube functionalization and polymer grafting: an ab-initio study, Journal of Physical Chemistry B 108 (2004) 15009–15012.

[32] Griebel, Michael and Hamaekers, Jan, Molecular dynamics simulations of the elastic moduli of polymer-carbon nanotube composites, Computer Methods in Applied Mechanics and Engineering 193 (17-20) (2004) 1773–1788.

[33] Brenner, D. W., Emperical potential for hydrocarbons for use in simulating the chemical vapor deposition of diamond films, Physical Review B 42 (1990) 9458–9471.

[34] Chandra, N. and Namilae, S. and Shet, C., Local elastic properties of carbon nanotubes in the presence of stone-wales defects, Physical Review B (Condensed Matter and Materials Physics) 69 (9) (2004) 094101–094112.

[35] Namilae, S. and Chandra, N. and Shet, C., Mechanical behavior of functionalized nanotubes, Chemical Physics Letters 387 (4-6) (2004) 247–252.

[36] Che, I. and Cagin, T. and W. A. Goddard, III, Studies of fullerenes and carbon nanotubes by an extended bond order potential, Nanotechnology 10 (1999) 263–268.

[37] Stuart, Steven J and Tutein, Alan B and Harrison, Judith A, A reactive potential for hydrocarbons with intermolecular interactions, The Journal of Chemical Physics 112 (14) (2000) 6472–6486.

[38] Meo, Michele and Rossi, Marco, Prediction of young's modulus of single wall carbon nanotubes by molecular-mechanics based finite element modelling, Composites Science and Technology 66 (11-12) (2006) 1597–1605.

[39] Collins, Philip G and Avouris, Phaedon, Nanotubes for electronics, Scientific American 283 (6) (2000) 62–69.

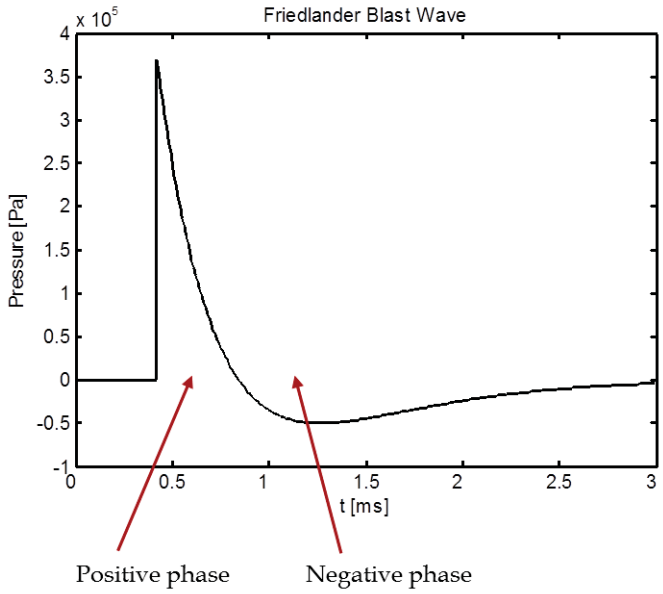

Figure 1: Representation of Friedlander Blast Wave

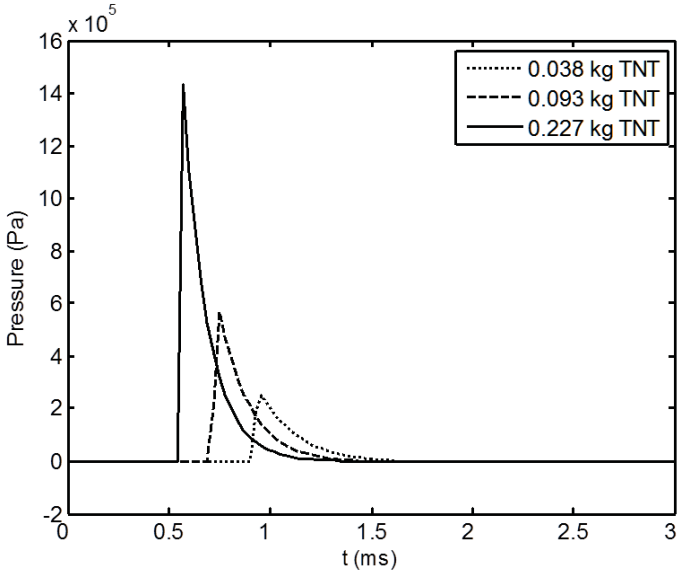

Figure 2: Conwep pressure applied at front of skull

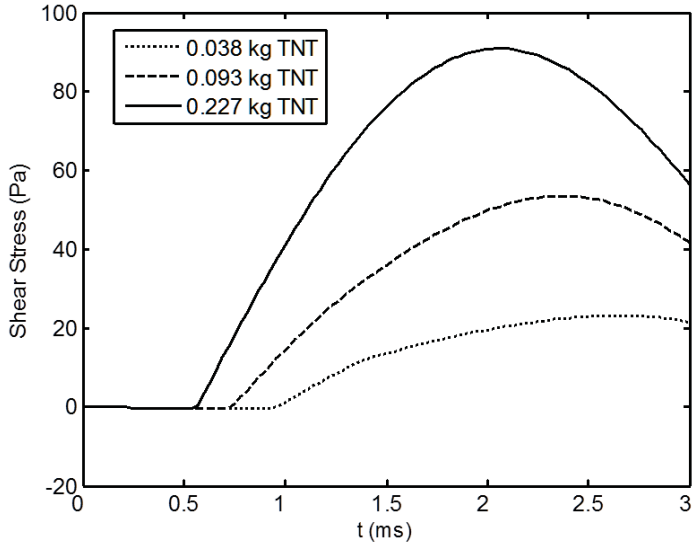

Figure 3: Shear stress for the unprotected head model for blast at the front of the brain

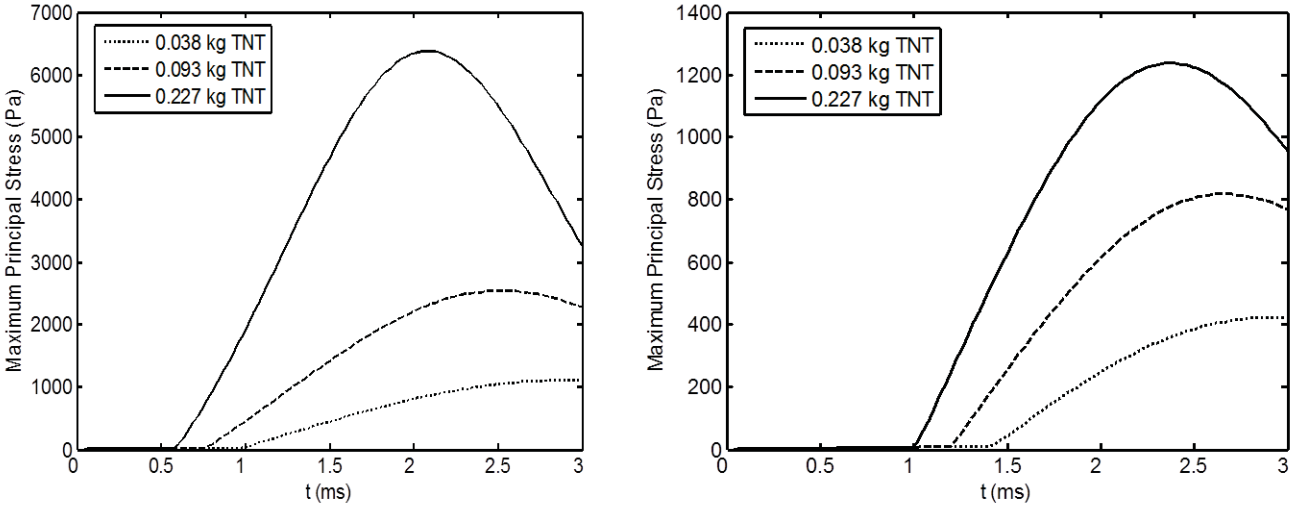

Figure 4: Principal stress in the brain at the (a) coup site and (b) counter coup site - for an unprotected rear detonations

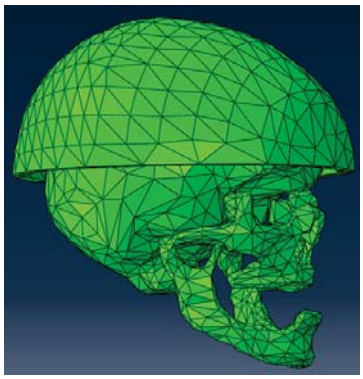

Figure 5: Finite element model of head with helmet

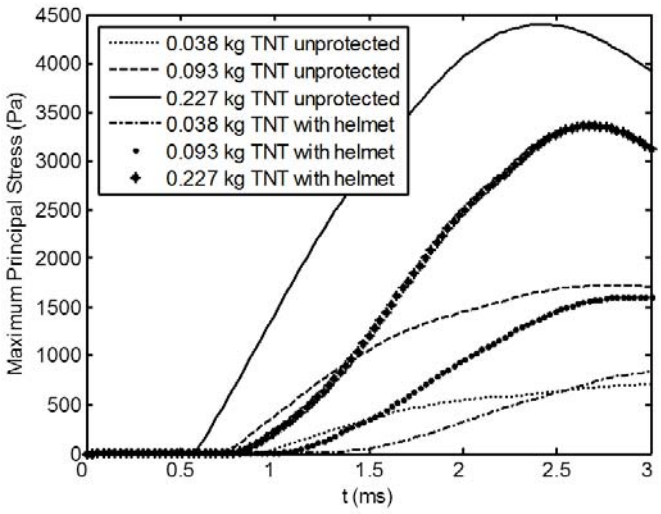

Figure 6: Maximum principal stress with and without helmet protection in the brain

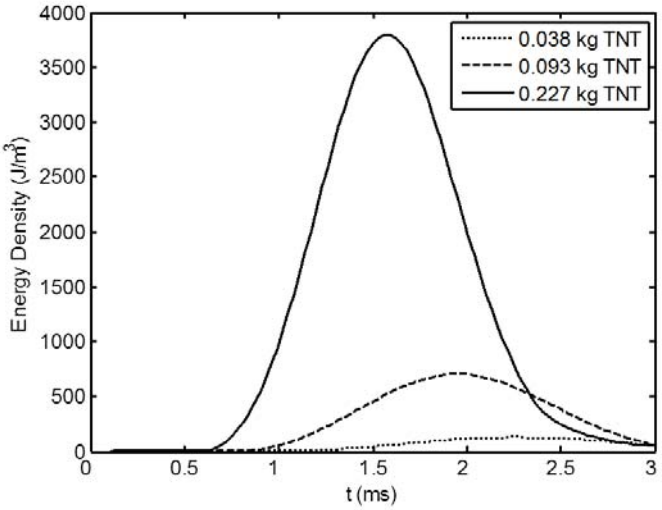

Figure 7: Energy density in the brain for the unprotected head model

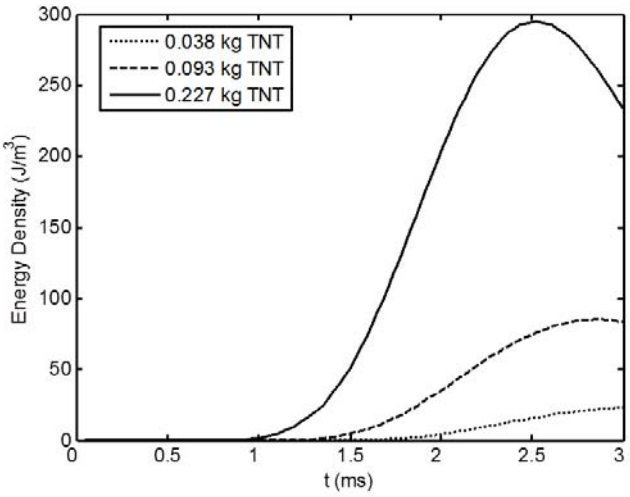

Figure 8: Energy density in the brain for the ACH-protected head model

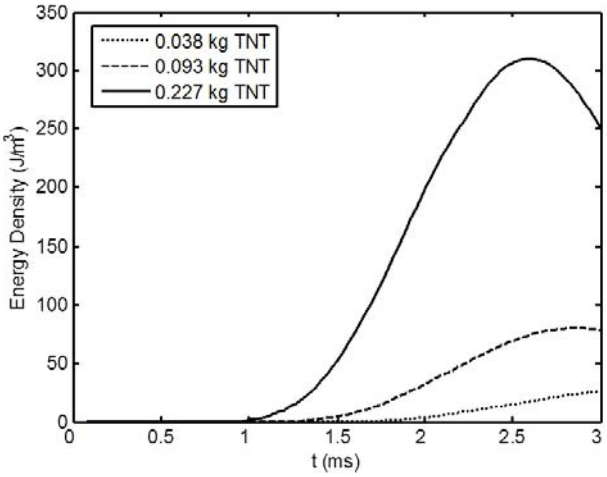

Figure 9: Energy density at the brain for the CNT-enhanced protected head model